Nanoscale

Pt−Co Truncated Octahedral Nanocrystals as a Highly Active and Durable Catalyst toward the Oxygen Reduction Reaction

Journal:	*Nanoscale*
Manuscript ID	NR-ART-04-2020-002904.R1
Article Type:	Paper
Date Submitted by the Author:	19-May-2020

Complete List of Authors:	Shen, Min; Georgia Institute of Technology, The Wallace H. Coulter Department of Biomedical Engineering; Fujian Institute of Research on the Structure of Matter, the Chinese Academy of Sciences, State Key Laboratory of Structural Chemistry Xie, Minghao; Georgia Institute of Technology, School of Chemistry and Biochemistry Slack, John; Vanderbilt University, Department of Chemical and Biomolecular Engineering Waldrop, Krysta; Vanderbilt University, Department of Chemical and Biomolecular Engineering Chen, Zitao; Georgia Institute of Technology, The Wallace H. Coulter Department of Biomedical Engineering Lyu, Zhiheng; Georgia Institute of Technology, School of Chemistry and Biochemistry Cao, Shaohong; Oak Ridge National Laboratory, Center for Nanophase Materials Sciences Zhao, Ming; Georgia Institute of Technology, School of Chemistry and Biochemistry Chi, Miaofang; Oak Ridge National Laboratory, Center for Nanophase Materials Sciences Pintauro, Peter; Vanderbilt University, Department of Chemical and Biomolecular Engineering Cao, Rong; Chinese Academy of Sciences Fujian Institute of Research on the Structure of Matter, Xia, Younan; Georgia Institute of Technology, The Wallace H. Coulter Department of Biomedical Engineering

Revised MS#NR-ART-04-2020-002904

Pt−Co Truncated Octahedral Nanocrystals: A Class of Highly Active and Durable Catalysts toward Oxygen Reduction

Min Shen,[a,b+] Minghao Xie,[c+] John Slack,[d] Krysta Waldrop,[d] Zitao Chen,[a] Zhiheng Lyu,[c] Shaohong Cao,[e] Ming Zhao,[c] Miaofang Chi,[e] Peter N. Pintauro,[d] Rong Cao,[b] and Younan Xia[a,c]*

[a]The Wallace H. Coulter Department of Biomedical Engineering, Georgia Institute of Technology and Emory University, Atlanta, Georgia 30332, United States

[b]State Key Laboratory of Structural Chemistry, Fujian Institute of Research on the Structure of Matter, Chinese Academy of Sciences, Fuzhou 350002, China

[c]School of Chemistry and Biochemistry, Georgia Institute of Technology, Atlanta, Georgia 30332, United States

[d]Department of Chemical and Biomolecular Engineering, Vanderbilt University, Nashville, Tennessee 37235, United States

[e]Center for Nanophase Materials Sciences, Oak Ridge National Laboratory, Oak Ridge, Tennessee 37831, United States

[+] These authors contributed equally to this work.

[*]Corresponding author. E-mail: younan.xia@bme.gatech.edu

Abstract

We report a facile and scalable synthesis of Pt−Co truncated octahedral nanocrystals (TONs) by employing $Pt(acac)_2$ and $Co(acac)_2$ as precursors, together with CO molecules and Mn atoms derived from the decomposition of $Mn_2(CO)_{10}$ as a reductant and a {111} facet-directing agent, respectively. Both the composition and yield of the Pt−Co TONs could be varied through the introduction of $CHCl_3$. When tested at 80 °C using membrane electrode assembly (MEA), the 4-nm $Pt_{2.6}Co$ TONs gave a mass activity of 294 A g_{Pt}^{-1} at beginning-of-life (BOL) and it increased to 384 A g_{Pt}^{-1} during recovery cycles. The mass activity at BOL only dropped by 24% after 30,000 voltage cycles at end-of-life (EOL) in a metal dissolution accelerated stress test. The $Pt_{2.6}Co/C$ catalyst outperformed the commercial TKK Pt_3Co/C (230 A g_{Pt}^{-1} at BOL and 40% loss after 30,000 cycles at EOL) in terms of both activity and durability. Our systematic analysis suggested that the enhancement in activity can be attributed to the combination of small, uniform size and well-defined {111} facets. This new class of catalysts holds promise for applications in proton-exchange membrane fuel cells.

KEYWORDS. bimetallic nanocrystal, oxygen reduction, electrocatalyst, membrane electrode assembly, fuel cell

Introduction

Proton-exchange membrane fuel cells (PEMFCs) are spectacular energy-conversion devices for both mobile and stationary applications because of their high energy and power densities, as well as the negligible emissions.[1–3] The sluggish oxygen reduction reaction (ORR) at the cathode of a PEMFC is a widely recognized factor that kinetically limits the conversion of chemical energy in a fuel to electrical power.[4–6] Such a limitation can be overcome through the use of a catalyst, and Pt-based nanoparticles have been the most viable catalyst toward ORR in terms of both activity and durability. However, the low abundance, limited supply, and increasing price intrinsically associated with Pt constantly present a barrier to the large-scale commercialization of PEMFCs.[7,8] To mitigate this issue, Pt−M (where M is typically a more abundant and less expensive transition metal such as Fe, Co, and Ni) alloy nanocrystals with controlled shapes have been extensively explored as the next-generation catalysts toward ORR. These catalytic materials have the capability to substantially improve the ORR activity while offering an avenue to reduce the Pt loading for cost-effective and sustainable products.[9,10]

Among various Pt−M alloys, the Pt−Co system has received considerable attention because of its relatively high ORR activity, long-term durability in an acidic medium, and low toxicity of the dissolved Co^{II} ions toward the polymer electrolyte.[11–13] In particular, Pt_3Co has been established as a superb ORR catalyst as it is located at the apex of the volcano plot of ORR activity to give an optimal oxygen absorption free energy (E_0) for achieving the highest specific activity.[2,11] The enhancement in catalytic performance can be attributed to both the ligand and strain effects. Regarding the ligand effect, it arises from the difference in electronegativity between Pt and Co for increasing the filling of the Pt *d*-band and thus downshifting the band's center. As for the strain effect, it involves a compressive lattice strain and thus shortening of the Pt−Pt bond distance on the surface when Co atoms with a smaller atomic radius are doped into the Pt lattice. Taken together, the E_0 of the oxygenated species (including -OH and -OOH) on the surface of the catalyst will be reduced relative to that of Pt, increasing the specific activity.[9,14]

The E_0 of Pt−M alloy nanocrystals can also be tuned by altering the surface structure (*i.e.*,

atomic arrangement), as typically achieved by controlling the geometric shape and thus the types of facets exposed on the surface. Using a related system, Stamenkovic and co-workers demonstrated that $Pt_3Ni(111)$ single crystals exhibited an ORR specific activity 10- and 90-fold, respectively, higher than those of Pt(111) single crystals and the state-of-the-art Pt/C catalyst in an aqueous $HClO_4$ solution.[15] Inspired by this result, a lot of efforts were made to synthesize Pt−Ni octahedral nanocrystals enclosed by {111} facets, attaining extremely high activity toward ORR.[10] In parallel, Park and co-workers successfully synthesized Pt_3Co truncated octahedra enclosed by a mix of {111} and {100} facets, which were found to exhibit enhanced ORR specific activity relative to that of Pt_3Co nanocubes, enclosed by {100} facets, in an aqueous $HClO_4$ solution.[16] This result indicated that the {111} facets of Pt−Co might be favorable for the achievement of high activity toward ORR. So far, a number of synthetic protocols have been developed for the preparation of Pt−Co alloy nanocrystals with well-defined shapes, such as cubes, cuboctahedra, and truncated octahedra, as well as those enclosed by high-index facets such as concave nanocubes, excavated octahedra, and nanowires.[10,16−20] However, many of the reported protocols for synthesizing Pt−Co nanocrystals enclosed by {111} facets involved the use of $Co_2(CO)_8$ or other zero-valent Co^0 complexes as the precursor, which is highly toxic and unstable in air or under light.[14,16] On the other hand, when Co^{II} or Co^{III} salts were used as a precursor, Pt−Co alloy nanocrystals encased by {100} facets were often obtained.[10,17,21,22] Taken together, there is still an urgent need to develop a facile and environmentally friendly protocol for the shape-controlled synthesis and scalable production of Pt−Co alloy nanocrystals mainly covered by {111} facets.

Despite the extensive exploration of Pt−Co alloy nanocrystals as catalysts toward ORR, it is worth pointing out that most of the tests were performed in the setting of a liquid half-cell at room temperature, rather than using a membrane electrode assembly (MEA) at 80 ^oC, which is more relevant to the operation of a PEMFC. As shown by recent studies of Pt-based polyhedral nanocrystals, those with particle sizes above 9 nm exhibited a significantly poorer ORR catalytic performance in MEA measurements than in liquid half-cell tests.[23,24] This difference can be

attributed to the stronger adsorption of SO_3^{2-} from solid-state Nafion-electrolyte on the Pt surface relative to that of ClO_4^-. In addition, the large particle size would result in a thicker catalyst layer on the catalyst-coated membrane of an MEA, adversely impacting the fuel cell performance. To address this issue, the catalytic particles should have a uniform size small enough to ensure satisfactory performance in fuel cells.

Herein, we developed a facile and scalable protocol for the synthesis of Pt−Co truncated octahedral nanocrystals (TONs) with a uniform edge length of *ca.* 4 nm and further explored them as an active and durable ORR catalyst under the condition of both liquid half-cell and fuel cell operations. Different from the reported 8-nm Pt_3Co TONs derived from the use of $Co_2(CO)_8$ as a metal carbonyl additive,[16] the current protocol used $Mn_2(CO)_{10}$ to generate Mn^0 and CO as the shape-directing and reducing agents, respectively. Significantly, the introduction of $CHCl_3$ could inhibit the formation of Pt–Mn alloy while tuning the yield and composition of the Pt−Co TONs by changing the coordination environments of Pt^{II} and Co^{II} ions.[25,26] Based on this strategy, Pt−Co TONs were synthesized with controlled sizes and compositions by adjusting the amounts of $Mn_2(CO)_{10}$ and/or $CHCl_3$ in the reaction mixture. When supported on carbon, the 4 nm Pt−Co TONs gave a mass activity of 310 A g_{Pt}^{-1} at 0.85 V in the liquid half-cell, together with a mass activity of 384 A g_{Pt}^{-1} at 0.9 V and 24 % loss after 30,000 cycles for the MEA test. All these data substantially surpassed those of a commercial TKK Pt_3Co/C.

Experimental section

Chemicals. Platinum(II) acetylacetonate ($Pt(acac)_2$, 97%), cobalt(II) acetylacetonate ($Co(acac)_2$, ≥99.0%), dimanganese(0) decacarbonyl ($Mn_2(CO)_{10}$, 98%), oleylamine (OAm, 70%), oleic acid (OAc, 90%), and benzyl ether (BE, 98%) were all obtained from Sigma-Aldrich. Chloroform ($CHCl_3$, ≥99.8%) was obtained from Merck KGaA. All chemicals were used as received.

Standard synthesis of 4-nm Pt−Co TONs. In a typical protocol, 120 mg of $Pt(acac)_2$ (0.31 mmol), 786 mg of $Co(acac)_2$ (3.1 mmol), 240 mg of $Mn_2(CO)_{10}$ (0.62 mmol), 12 mL of

OAm, 6.0 mL of OAc, 4.0 mL of $CHCl_3$, and 42 mL of BE were mixed in a 250-mL 2-neck flask and heated to 60 °C under magnetic stirring and argon protection for the dissolution of solids and removal of oxygen. After 40 min, argon purging was stopped, and the reaction container was transferred into an oil bath for heating at 230 °C for 50 min. The reaction mixture was cooled down to room temperature naturally, and the Pt−Co TONs were precipitated out by sequentially adding toluene (30 mL) and acetone (90 mL). The supernatant was removed by centrifugation at 12,000 rpm for 10 min. The as-obtained Pt−Co TONs could be easily re-dispersed in toluene.

Preparation of Pt−Co TONs/C. A suspension of the Pt−Co TONs in toluene was mixed with 100 mg of Ketjen Black (KB) carbon suspended in toluene under ultrasonication for 10 min to achieve a Pt loading of *ca.* 17.6 wt%. The mixture was continued with magnetic stirring and ultrasonication for 3 h. The resulting Pt−Co TONs/C was centrifuged at 12,000 rpm for 15 min, washed 3 times with ethanol and water, respectively, and finally dried for 30 min in an oven at 70 °C prior to ORR measurements.

Morphological, structural, and elemental characterizations. Transmission electron microscopy (TEM) images were taken using a HT7700 microscope (Hitachi, Tokyo, Japan) operated at 120 kV by drop casting the nanoparticle dispersions on carbon-coated copper grids and drying under ambient conditions. High-resolution TEM (HRTEM), high-angle annular dark-field scanning TEM (HAADF-STEM), and energy dispersive X-ray (EDX) mapping analyses were performed using an aberration-corrected Hitachi HD2700 STEM at the Institute for Electronics and Nanotechnology (IEN, Georgia Institute of Technology) and a Cs-corrected FEI Titan 80/300 kV TEM/STEM at Oak Ridge National Laboratory (ORNL). The metal contents in the as-obtained catalysts were determined using an inductively-coupled plasma mass spectrometer (ICP-MS, Perkin–Elmer, NexION 300Q). X-ray diffraction (XRD) patterns were recorded with a PANalytical X'Pert PRO Alpha-1 diffractometer using 1.8 kW Ceramic Copper tube source. X-ray photoelectron spectroscopy (XPS) measurements were carried out using a spectrometer (Thermo Scientific, K-Alpha) with Al Kα X-ray (1486.6 eV) as the light source.

Catalyst ink preparation and electrochemical measurements. Approximately 2.0 mg of

the Pt−Co TONs/C catalyst was dispersed in a mixture of water (1 mL), isopropanol alcohol (1 mL), and 8 μL of 5 wt% Nafion (Aldrich) under ultrasonication for 30 min. The concentration of Pt in the final dispersion was determined using an ICP-MS. 10 μL of this suspension was deposited on a pre-cleaned glassy carbon electrode (Pine Instruments) and allowed to dry under ambient conditions. For commercial Pt/C catalyst (20 wt% 3.2 nm nanoparticles on Vulcan XC-72 carbon support, Premetek Co.) and Pt_3Co/C catalyst (48.6 wt%, TEC36E52, Tanaka Kikinzoku), the amounts of Pt loading were 2 μg. A HydroFlex reference electrode (ET070, Edaq Inc.) and Pt mesh were used as the reference and counter electrodes, respectively. The potentials of the reference electrode were calibrated using a home-built reversible hydrogen electrode (RHE).

After loading, the working electrode was cycled in a N_2-saturated 0.05 M H_2SO_4 (GFS Chemicals) solution for 20 cycles between 0.05 and 1.2 V at a scanning rate of 100 mV s^{-1} until a stable cyclic voltammetry (CV) curve was obtained. The electrochemical active surface area (ECSA) of the catalyst is calculated by measuring the average charges associated with the adsorption and desorption of hydrogen between 0.05 and 0.4 V, assuming 210 μC/cm^2 for a monolayer of adsorbed hydrogen on Pt surface. Double-layer correction was applied. The oxygen reduction polarization curves were measured in an O_2-saturated 0.05 M H_2SO_4 solution at a scan rate of 20 mV s^{-1} and a rotation speed of 1,600 rpm. The kinetic current density j_k at 0.9 V was derived from the Koutecky−Levich equation:

$$\frac{1}{j} = \frac{1}{j_k} + \frac{1}{B\omega^{1/2}}$$

Where j is the measured current density, B is a constant, and ω is the rotation speed. The electrochemical measurements were performed using a CHI600E potentiostat (CH Instrument, Austin, TX).

Membrane electrode assembly (MEA) fabrication and fuel cell testing. Spray inks were prepared by dispersing a carbon-supported catalyst with Nafion dispersion (Liquion 1115 1100 EW). The tested catalysts included 17.6 wt% Pt−Co TONs/C, 20 wt% Pt/C (Premetek Co.), and 48.6 wt% Pt_3Co/C (TEC36E52, Tanaka Kikinzoku). Spray inks were prepared at Vanderbilt

University by the following steps. Typically, the catalyst inks were made by mixing water, n-propanol, and Nafion ionomer dispersion (20 wt%). The mass-based ionomer/carbon (I/C) ratio in the ink was kept at a constant of 1.2, and the water/alcohol weight ratio was set to 1.5. The ink was well-mixed using a homogenizer (Ika T25) for 4 h. Then, the electrocatalyst cathode layer was formed on gas diffusion layers (GDLs, Sigracet 29BC) using an automated robotic spray system (Asymtek, Nordson). The slurry anode was prepared by dispersing TKK Pt/C in a mixture of water, n-propanol, and H^+ Nafion solution (20 wt%). The mass ratio between TKK Pt/C and H^+ Nafion was 65:35. The MEAs were fabricated using the spray-coating method on an as-received Nafion 211 membrane. The active area was 5 cm^2. The catalyst loading was fixed at 0.1 mg_{Pt} cm^{-2} for both electrodes. The MEAs were hot-pressed at 150 °C using a pressure of 20 kg cm^{-2} for 4 min. The MEA tests were conducted at 80 °C. The anode and cathode were supplied with H_2 and air at a constant stoichiometry of 2 and 2 under a backpressure of 170 kPa_{abs}. The measurements were carried out at 100% relative humidity (RH).

To simulate acceleration/deceleration events in an automotive setting, the fuel cell commercialization conference of Japan (FCCJ) established a square-wave voltage cycling protocol from 0.6 V to 0.95 V. This cycling subjects the catalyst particles to electrochemical degradation such as formation of platinum oxide species, agglomeration of particles in the catalyst layer by Ostwald ripening, and migration/isolation of particles into the membrane. The protocol involved the use of 100% RH, together with the feeding of 100 sccm H_2 (anode) and 100 sccm N_2 (cathode). An external potentiostat was used to apply 0.6 V for 3 s and then 0.95 V for 3 s, constituting one cycle of 6 s. Tests were carried out using a Gamry Instruments Reference 3000 Potentiostat. According to the recommendation from the United States Department of Energy, the accelerated stress test (AST) was applied for 30,000 cycles between 0.6 and 0.95 V vs RHE.

Results and discussion

Synthesis and characterizations of the Pt−Co TONs. Fig. 1A shows a TEM image of the

Pt−Co TONs synthesized using the standard protocol. They had an average edge length of 4.3 ± 0.5 nm (Fig. S1), together with a truncated octahedral shape in high purity. The small size and high uniformity can be attributed to the fast initial reduction rate during the nucleation stage in the presence of $CHCl_3$. Previous studies indicated that OAm could serve as a coordination ligand to lower the reduction potential of Pt^{II} in addition to its role as a surface stabilizer.[27,28] The introduction of $CHCl_3$ made the reaction much faster because $CHCl_3$ could react with OAm though a coupling reaction for the generation of R-$NHCHCl_2$.[25] Upon coupling with -$CHCl_2$, the amine group in OAm would experience a stronger steric hindrance, weakening its coordination with Pt^{II} ions. As such, the reduction potential of Pt^{II} would not be reduced relative to the case of pure OAm, helping increase the reduction rate of the precursor in the initial stage of nucleation.[27,29] Due to the formation of a large number of seeds with a narrow distribution in size, the final nanocrystals could be kept small and uniform. The nanocrystals tended to self-assemble into an ordered array due to their high uniformity, as well as the presence of OAm on the surface. Fig. 1, B and C, shows the HAADF-STEM image taken along the [011] zone axis of an individual particle, indicating a single-crystal structure enclosed by {111} and {100} facets, together with truncated corners. The *d*-spacing between adjacent lattice fringes of the {111} planes was smaller than that of the {111} planes of face-centered cubic (*fcc*) bulk Pt (2.2 *versus* 2.3 Å). The energy-dispersive X-ray (EDX) spectroscopy mapping reveals that both Pt and Co were uniformly distributed throughout the particle, confirming the formation of an alloy composition (Fig. 1, D−F).

The success of our synthesis critically relied on the use of $Mn_2(CO)_{10}$ as a metal carbonyl additive. To reveal the explicit role(s) played by $Mn_2(CO)_{10}$ in the synthesis, a set of control experiments were conducted by adding different amounts of $Mn_2(CO)_{10}$ into the reaction mixture of a standard synthesis. As shown in Fig. 2, when the amount of $Mn_2(CO)_{10}$ was reduced from 240 to 180, 120, and 60 mg, Pt−Co TONs with average edge lengths of 4.8, 5.2, and 5.8 nm were obtained, respectively, while their elemental compositions were kept essentially the same. These results indicate that the size of the Pt−Co TONs could be readily tuned by varying the amount of

$Mn_2(CO)_{10}$ introduced into the reaction system. Under the reaction condition, $Mn_2(CO)_{10}$ would decompose immediately to generate CO, a reducing agent. When the amount of $Mn_2(CO)_{10}$ was reduced, the reduction of Pt^{II} and Co^{II} precursors would be slowed down, generating fewer seeds. As a result, the size of the Pt−Co TONs would be increased.

It was demonstrated that an effective means to control the shape of metal nanocrystals is to introduce foreign metal ions or atoms through *in situ* decomposition of a carbonyl compound. For example, Ag^{I} ions and Fe^{II}/Fe^{III} have been applied to alter the shape of Pt nanocrystals,[30,31] Similarly, $Fe(CO)_5$ has been employed to manipulate the shape of PtFe[32] and Pt[33] nanocrystals. In the present work, we found that the presence of $Mn_2(CO)_{10}$ was key to controlling the shape of the Pt−Co nanocrystals. As a product from the decomposition of $Mn_2(CO)_{10}$, Mn^0 could serve as a shape-directing agent for the formation of Pt−Co TONs in two plausible scenarios.[25] In the first case, the Mn atoms were preferentially deposited on the Pt-Co{100} facets and then reacted with the precursors to generate Pt and Co atoms through galvanic replacement. As a result, the nanocrystals preferentially grew along the <100> directions for the exposure of {111} facets. In the second scenario, the Mn atoms could selectively adsorb onto the Pt-Co{111} facets to lower their surface energy, leading to the formation of nanocrystals covered by {111} facets. It should be pointed out that neither one of these mechanisms is supported by solid experimental data. The presence of truncated corners as {100} facets could be ascribed to the small size of the nanocrystals and/or the inadequate amount of $Mn_2(CO)_{10}$. This argument was supported by the emergence of Pt−Co truncated cubes when the amount of $Mn_2(CO)_{10}$ was reduced to 60 mg (Fig. 2D). For the as-synthesized standard sample, the Mn 2p signal (Mn $2p_{1/2}$ at 650.26 eV and Mn $2p_{3/2}$ at 638.52 eV) was essentially negligible in the XPS spectrum (Fig. S2A), indicating that only a limited number of Mn atoms were incorporated into the crystal lattice of the Pt−Co TONs under the experimental conditions used.

As a parameter key to the decomposition of $Mn_2(CO)_{10}$ and the reaction kinetics, the reaction temperature was also optimized. When the reaction temperature was changed from 230 to 180 and 210 °C, the Pt/Co atomic ratios of the as-obtained Pt−Co TONs increased from 2.6 to

4.4 and 3.8, respectively, based on ICP-MS analysis. This change might result from the slower reduction rate of $Co(acac)_2$ at a lower temperature. Moreover, the average size (5.5 ± 0.5 nm) of the particles obtained at 180 °C was larger than the samples prepared using either 210 or 230 °C, probably due to the slower reduction of $Pt(acac)_2$ at a lower temperature and thus the formation of fewer seeds (Fig. S3).

In the current synthesis, $CHCl_3$ was crucial for controlling both the yield and composition of the products. Fig. 3A shows their correlations at two different Pt/Co feeding ratios. According to the ICP-MS data, the product yields were 34, 36, 43, and 59% when the introduced volumes of $CHCl_3$ were 3, 4, 5, and 6 mL, respectively, at a Pt/Co molar feeding ratio of 1:10. When the feeding ratio was changed to 1:15, the corresponding product yields became 36, 38, 43, and 54%, respectively. The variation in product yield can be attributed to the positive correlation between the reduction rate and the amount of $CHCl_3$. As mentioned above, the R-$NHCHCl_2$ produced from the coupling reaction would coordinate to Pt^{II} ions more weakly than pure OAm, generating Pt atoms at a faster rate and thus achieving a higher product yield.[25,26] The use of $CHCl_3$ could also control the Pt/Co atomic ratio by decreasing the amount of Co^{II} precursor involved in the reaction (Fig. 3A and Table S1). As a by-product of the coupling reaction, HCl could further react with $Co(acac)_2$, generating $CoCl_2$ that was insoluble in BE. As a result, when increasing the amount of $CHCl_3$, the Co^{II} precursor available to the synthesis would drop, generating Pt−Co nanocrystals with higher Pt/Co atomic ratios. As shown by the XRD patterns in Fig. 3B, the as-obtained Pt−Co nanocrystals featured an *fcc* structure. The diffraction peaks were gradually shifted to higher 2θ values relative to those of *fcc*-Pt (JCPDS #04-0802) as the Co content in the particles was increased. The shift in peak position can be attributed to the substitution of Pt atoms with smaller Co atoms (atomic radius: 1.39 *vs.* 1.26 Å) in the crystal lattice, resulting in the reduction in lattice spacing for the nanocrystals.

The electronic structures and surface cleanness of the Pt−Co TONs were further studied by XPS. As shown in Fig. S2B, the Pt 4f spectrum confirmed that the as-obtained sample was dominated by zero-valent Pt. In addition, the bind energy of Pt 4f peaks was positively shifted by

0.4 eV compared to that of pure Pt (Pt $4f_{5/2}$ at 74.41 eV and Pt $4f_{7/2}$ at 70.96 eV) because the alloying of Pt with another metal could alter the electronic structure of the Pt.[34] In terms of the Co 2p spectrum (Fig. S2C), the co-presence of zero-valent Co (Co $2p_{1/2}$ at 793.29 eV and Co $2p_{3/2}$ at 778.08 eV) and Co^{II} (Co $2p_{1/2}$ at 798.14 eV and Co $2p_{3/2}$ at 782.03 eV) corresponded to the Co atoms incorporated in the Pt lattice and Co^{II} complexes on the surface of the nanocrystals, respectively. The peaks of Co^{II} mainly came from the unreacted Co^{II} precursor and $CoCl_2$. Moreover, the barely observed N 1s peak (398.52 eV) from OAm indicated that the surface of the Pt−Co TONs was relatively clean (Fig. S2D). Our previous work indicated that the introduction of a suitable solvent could significantly reduce the surface coverage of surfactants.[34] For our synthesis, we believe that the use of BE could ensure low coverage densities for both OAm and OAc while producing a truncated octahedral shape for the Pt−Co nanocrystals.

ORR performance in the liquid half-cell. The electrochemical performance of the 4-nm Pt−Co TONs (loaded on carbon, Fig. S4, denoted $Pt_{2.6}Co$ TONs/C) was benchmarked against Premetek Pt/C and TKK Pt_3Co/C using the rotating disk electrode (RDE) technique. Cyclic voltammetry was applied to measure the ECSAs of the catalysts, and the values for $Pt_{2.6}Co$ TONs/C, Premetek Pt/C, and TKK Pt_3Co/C catalysts were 23.8, 25.1, and 20.1 $m^2\ g_{Pt}^{-1}$, respectively (Fig. 4, A and B). Fig. 4C shows the positive-going ORR polarization curves of the catalysts. Following the Koutecky−Levich equation, the kinetic current densities of the ORR polarization curves were calculated and normalized against the ECSA and Pt mass to attain the corresponding specific and mass activities ($j_{k,\text{specific}}$ and $j_{k,\text{mass}}$), respectively. It is worth pointing out that the kinetic currents in our study were not iR-corrected.[35]

Table S2 shows a summary of the calculated specific and mass activities of the catalysts. The $Pt_{2.6}Co$ TONs/C exhibited a specific activity of 1.30 mA cm^{-2} at 0.85 V *vs.* RHE, which was higher than that of the Premetek Pt/C (0.84 mA cm^{-2}). The enhancement in specific activity for $Pt_{2.6}Co$ TONs/C can be attributed to the compressive surface strain arising from the difference in lattice constant between Pt and Co, as well as the ligand effect from the electronic coupling between the two elements.[36] The compressive lattice strain would shorten the Pt−Pt bond and

down-shift the *d*-band center of Pt, resulting in weaker adsorption for the OH_{ad} species. In addition, the ligand effect between Pt and Co could further modify the electronic structure of Pt, as revealed by the increase in binding energy for the Pt 4f XPS peaks relative to those of pure Pt (Fig. S2B). The positive shift in binding energy further weakened the interactions between Pt and OH_{ad} species, resulting in enhanced activity toward ORR.[34,15,17] The specific activity of $Pt_{2.6}Co$ TONs/C was slightly lower than that of TKK Pt_3Co/C (1.34 mA cm^{-2}) (Fig. S5). This was possibly due to the remaining stabilizers on the surface of $Pt_{2.6}Co$ TONs, which might block some of the active sites on the surface and thus lowered the specific activity. As shown in Fig. 4D, the mass activity of $Pt_{2.6}Co$ TONs/C was 310 A g_{Pt}^{-1} at 0.85 V, which was higher than those of Premetek Pt/C catalyst (210 A g_{Pt}^{-1}) and TKK Pt_3Co/C (270 A g_{Pt}^{-1}). The enhancement in mass activity for $Pt_{2.6}Co$ TONs/C can be attributed to the small and uniform size, well-defined facets, and optimal composition of the catalyst.

MEA performance in the fuel cell. We then applied the 4-nm $Pt_{2.6}Co$ TONs/C catalyst in MEA to evaluate its ORR performance in a fuel cell. As shown in Fig. 5A, the mass activity and ECSA of $Pt_{2.6}Co$ TONs/C at beginning-of-life (BOL) were 294 A g_{Pt}^{-1} and 99 m^2 g_{Pt}^{-1}, respectively. A recovery protocol was conducted to recover the voltage loss and mass activity reduction arising from contamination to the Pt surface by the ionomer.[37] During the six runs of recovery, we observed a maximum mass activity in the 4th recovery cycle at a value of 384 A g_{Pt}^{-1}, and its corresponding maximum power density and power density at 0.65 V were 702 and 612 mW cm^{-2}, respectively (Fig. 5B). The durability of $Pt_{2.6}Co$ TONs/C was also tested in MEA using an accelerated stress test (AST) for 30,000 cycles based on the protocol from the DOE/fuel cell technologies team.[38] We collected the H_2/air polarization curves and corresponding parameters after 1,000, 5,000, 10,000, and 30,000 cycles, respectively (Table S3). As shown in Fig. 5C, the $Pt_{2.6}Co$ TONs/C showed a minor performance loss in the high-current density region (>1000 mA cm^{-2}). This might be caused by the increase in mass transport resistance due to the change in porosity and interruption of the three-phase interface between the catalyst, carbon support, and ionomer.[23,39] Fig. 5D shows the changes in mass activity and ECSA after different

cycles of AST. The $Pt_{2.6}Co$ TONs/C exhibited 24% mass activity loss and 17% ECSA drop in terms of BOL and end-of-life (EOL), together with experimentally calculated 10 mV open circuit voltage (OCV) loss and 4.1% maximum power density loss (Table S4). This performance meets the DOE 2020 target on durability set for catalyst (<40% loss in mass activity). Both the slight decay of polarization curves, as well as the slow drops in mass activity and ECSA during AST indicated that the 4-nm $Pt_{2.6}Co$ TONs/C catalyst was exceptionally stable under laboratory fuel cell operation that mimics the conditions typical of automotive applications.

The MEA performance of $Pt_{2.6}Co$ TONs/C was also compared with that of TKK Pt_3Co/C in the low-current density region (<1000 mA cm^{-2}), where the performance (i.e., OCV loss) is determined by the intrinsic ORR activity of the cathode catalyst and gas cross-over. As shown in Fig. 5E, the polarization curve of $Pt_{2.6}Co$ TONs/C at BOL exhibited a higher current density at 0.6 V than that of TKK Pt_3Co/C, indicating a better ORR performance of the $Pt_{2.6}Co$ TONs/C under the same fuel cell conditions. After 30,000 cycles of AST, the polarization curve of $Pt_{2.6}Co$ TONs/C showed much better performance than that of TKK Pt_3Co/C, demonstrating an excellent stability (Fig. 5F). The mass activity of $Pt_{2.6}Co$ TONs/C at EOL was 224 A g_{Pt}^{-1}, which was still much greater than that of TKK Pt_3Co/C at EOL (138 A g_{Pt}^{-1}). The corresponding power density plots of $Pt_{2.6}Co$ TONs/C and TKK Pt_3Co/C at BOL and EOL are shown in Fig. 5, E and F, respectively. After 30,000 cycles of AST, the maximum power density of TKK Pt_3Co/C dropped from 593 to 247 mW cm^{-2} (Table S4). In contrast, the maximum power density of $Pt_{2.6}Co$ TONs/C barely changed, featuring a value of 707 mW cm^{-2} at BOL and 678 mW cm^{-2} at EOL. Collectively, these results indicate that the $Pt_{2.6}Co$ TONs hold great promise for use as a cathode catalyst in commercial PEMFCs.

Conclusions

In summary, we have developed a one-pot protocol for the facile and scalable production of Pt−Co TONs with tunable sizes and compositions. The size could be controlled by changing the amount of $Mn_2(CO)_{10}$ added, whereas the composition and yield of the nanocrystals were mainly

determined by the volume of $CHCl_3$ introduced into the reaction mixture. The as-obtained Pt−Co TONs exhibited an enhanced ORR activity relative to both Premetek Pt/C and TKK Pt_3Co/C in the liquid half-cell test. Significantly, the trend in ORR activities could be successfully translated into satisfactory MEA performance for Pt−Co TONs, giving a mass activity of 384 A g_{Pt}^{-1} at 80 ^{o}C, together with only 24% loss after 30,000 cycles of the AST. Both the catalytic activity and durability exceeded those of commercial TKK Pt_3Co/C under the same testing conditions. The enhanced performance was believed to originate from a reduced particle size and thus enlarged ECSA, as well as well-defined facets on the Pt−Co TONs. It is expected that this new class of Pt−Co catalysts will offer a strong candidate for application in PEMFCs.

Associated content

Supporting information

Electronic Supplementary Information (ESI) available: Fig. S1−S5, Table S1−S4, TEM images, XPS, electrochemical data, and fuel cell performance of the catalyst. See DOI: xx

Author information

Corresponding author

*E-mail: younan.xia@bme.gatech.edu.

Conflict of interest

There are no conflicts of interest to declare.

Acknowledgements

This work was supported in part by a consortium grant from the DOE (DE-EE-0007653) and start-up funds from the Georgia Institute of Technology. TEM imaging, high-resolution TEM imaging, XRD, and XPS analyses were performed at the Georgia Tech Institute for Electronics and Nanotechnology, a member of the National Nanotechnology Coordinated Infrastructure,

which is supported by the NSF (Grant ECCS-1542174). The STEM and EDX characterizations were performed at the Oak Ridge National Laboratory's Center for Nanophase Materials Sciences, which is a DOE Office of Science User Facility.

References

(1) F. T. Wagner, B. Lakshmanan and M. F. Mathias, *J. Phys. Chem. Lett.*, 2010, **1**, 2204−2219.

(2) O. T. Holton and J. W. Stevenson, *Platin. Met. Rev.*, 2013, **57**, 259−271.

(3) Y. Wang, K. Chen, J. Mishler, S. C. Cho and X. C. Adroher, *Appl. Energ.*, 2011, **88**, 981−1007.

(4) M. K. Debe, *Nature*, 2012, **486**, 43−51.

(5) H. A. Gasteiger and N. M. Markovic, *Science*, 2009, **324**, 48−49.

(6) X. Wang, M. T. Swihart and G. Wu, *Nat. Catal.*, 2019, **2**, 578−589.

(7) A. Chen and P. Holt-Hindle, *Chem. Rev.*, 2010, **110**, 3767−3804.

(8) B. C. H. Steele and A. Heinzel, *Nature*, 2001, **414**, 345−352.

(9) J. Greeley, I. E. L. Stephens, A. S. Bondarenko, T. P. Johansson, H. A. Hansen, T. F. Jaramillo, J. Rossmeisl, I. Chorkendorff and J. K. Norskov, *Nat. Chem.*, 2009, **1**, 552−556.

(10) Y. Wang, N. Zhao, B. Fang, H. Li, X. T. Bi and H. Wang, *Chem. Rev.*, 2015, **115**, 3433−3467.

(11) V. R. Stamenkovic, B. S. Mun, M. Arenz, K. J. J. Mayrhofer, C. A. Lucas, G. Wang, P. N. Ross and N. M. Markovic, *Nat. Mater.*, 2007, **6**, 241−247.

(12) E. Antolini, J. R. C. Salgado and E. R. Gonzalez, *J. Power. Sources*, 2006, **160**, 957−968.

(13) X. Li, H. R. Colon-Mercado, G. Wu, J. W. Lee and B. N. Popov, *Electrochem. Solid St.*, 2007, **10**, B201−B205.

(14) C. Wang, N. M. Markovic and V. R. Stamenkovic, *ACS Catal.*, 2012, **2**, 891−898.

(15) V. R. Stamenkovic, B. Fowler, B. S. Mun, G. Wang, P. N. Ross, C. A. Lucas and N. M. Markovic, *Science*, 2007, **315**, 493−497.

(16) S. I. Choi, R. Choi, S. W. Han and J. T. Park, *Chem−Eur. J.*, 2011, **17**, 12280−12284.

(17) J. Wu and H. Yang, *Accounts Chem. Res.*, 2013, **46**, 1848−1857.

(18) Y. Qin, X. Zhang, X. Dai, H. Sun, Y. Yang, X. Li, Q. Shi, D. Gao, H. Wang, N. Yu and S. Sun, *Small*, 2016, **12**, 524−533.

(19) Q. Chen, Z. Cao, G. Du, Q. Kuang, J. Huang, Z. Xie and L. Zheng, *Nano Energy*, 2017, **39**, 582−589.

(20) L. Bu, S. Guo, X. Zhang, X. Shen, D. Su, G. Lu, X. Zhu, J. Yao, J. Guo and X. Huang, *Nat. Commun.*, 2016, **7**, 1−10.

(21) J. Wu, A. Gross and H. Yang, *Nano Lett.*, 2011, **11**, 798−802.

(22) H. Yang, J. Zhang, K. Sun, S. Zou and J. Fang, *Angew. Chem., Int. Ed.*, 2010, **49**, 6848−6851.

(23) J. Li, Z. Xi, Y. Pan, J. S. Spendelow, P. N. Duchesne, D. Su, Q. Li, C. Yu, Z. Yin, B. Shen, Y. S. Kim, P. Zhang and S. Sun, *J. Am. Chem. Soc.*, 2018, **140**, 2926−2932.

(24) Y. Wang, W. Long, L. Wang, R. Yuan, A. Ignaszak, B. Fang and D. P. Wilkinson, *Energ. Environ. Sci.*, 2018, **11**, 258−275.

(25) Y. Kang, J. B. Pyo, X. Ye, R. E. Diaz, T. R. Gordon, E. A. Stach and C. B. Murray, *ACS Nano*, 2013, **7**, 645−653.

(26) C. Desmarets, R. Schneider and Y. Fort, *Tetrahedron Lett.*, 2001, **42**, 247−250.

(27) K. Ahrenstorf, H. Heller, A. Kornowski, J. A. C. Broekaert and H. Weller, *Adv. Funct. Mater.*, 2008, **18**, 3850−3856.

(28) J. Zhang, H. Yang, J. Fang and S. Zou, *Nano Lett.*, 2010, **10**, 638−644.

(29) H. Zheng, R. K. Smith, Y. Jun, C. Kisielowski, U. Dahmen and A. P. Alivisatos, *Science*, 2009, **324**, 1309−1312.

(30) H. Song, F. Kim, S. Connor, G. A. Somorjai and P. Yang, *J. Phys. Chem. B*, 2005, **109**, 188−193.

(31) J. Chen, T. Herricks and Y. Xia, *Angew. Chem., Int. Ed.*, 2005, **44**, 2589−2592.

(32) M. Chen, J. Kim, J. Liu, H. Fan and S. Sun, *J. Am. Chem. Soc.*, 2006, **128**, 7132−7133.

(33) C. Wang, H. Daimon, T. Onodera, T. Koda and S. Sun, *Angew. Chem., Int. Ed.*, 2008, **47**,

3588−3591.

(34) S. I. Choi, S. Xie, M. Shao, J. H. Odell, N. Lu, H. Peng, L. Protsailo, S. Guerrero, J. H. Park, X. Xia, J. Wang, M. J. Kim and Y. Xia, *Nano Lett.*, 2013, **13**, 3420−3425.

(35) S. Mukerjee, S. Srinivasan, M. P. Soriaga and J. Mcbreen, *J. Electrochem. Soc.*, 1995, **142**, 1409−1422.

(36) D. S. Choi, A. W. Robertson, J. H. Warner, S. O. Kim and H. Kim, *Adv. Mater.*, 2016, **28**, 7115−7122.

(37) J. Zhang, B. A. Litteer, F. D. Coms and R. Makharia, *J. Electrochem. Soc.*, 2012, **159**, F287−F293.

(38) W. Jung, T. Xie, T. Kim, P. Ganesan and B. N. Popov, *Electrochim. Acta*, 2015, 167, 1−12.

(39) Y. S. Kim, C. F. Welch, N. H. Mack, R. P. Hjelm, E. B. Orler, M. E. Hawley, K. S. Lee, S. D. Yim and C. M. Johnston, *Phys. Chem. Chem. Phys.*, 2014, **16**, 5927−5932.

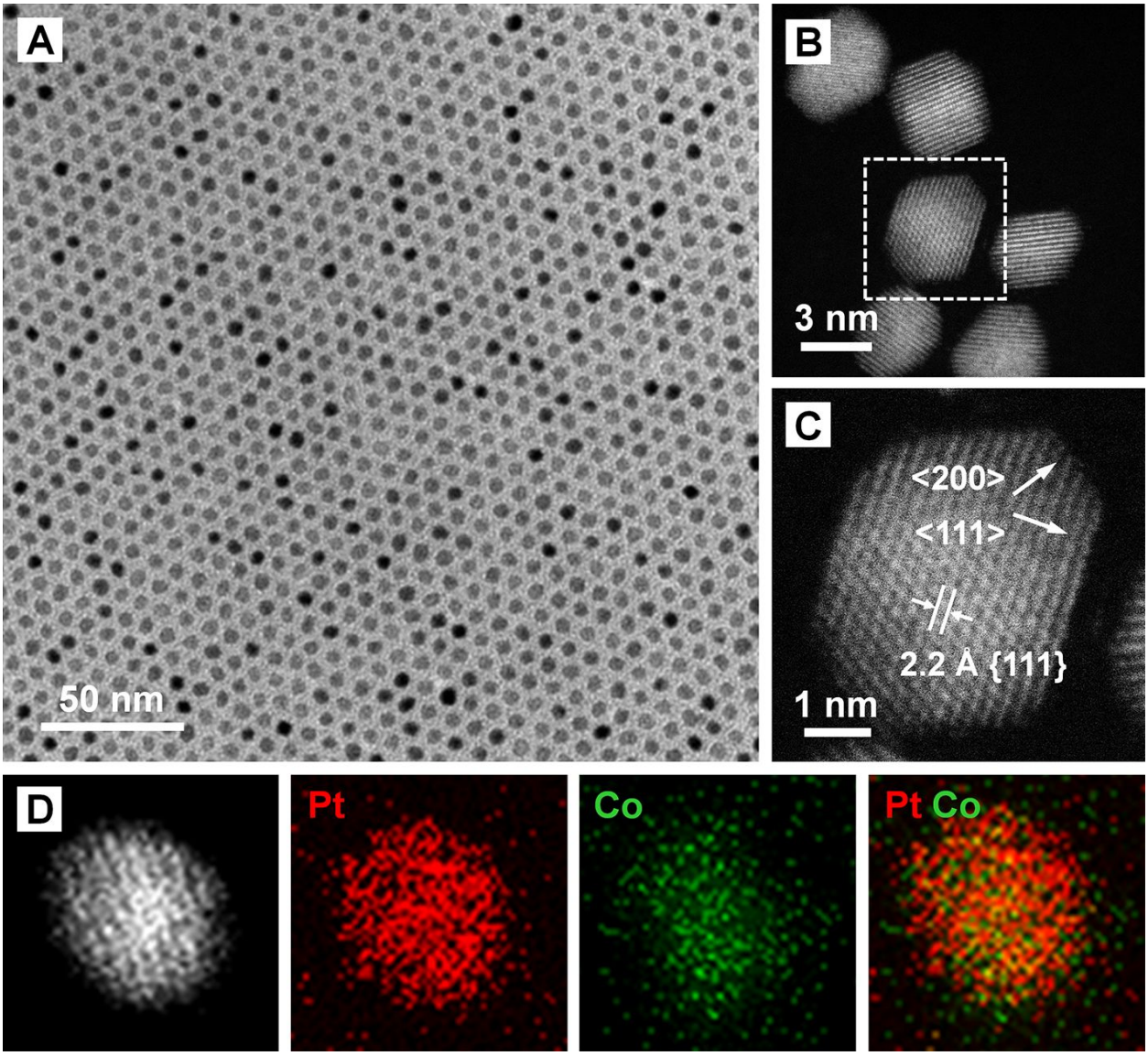

Fig. 1. (A) TEM and (B) HAADF-STEM images of the Pt−Co TONs synthesized using the standard protocol. (C) Atomic-resolution HAADF-STEM image recorded from an individual particle, as marked by a box in panel (B). (D) HAADF-STEM image and EDX mapping of the elemental distributions of another particle.

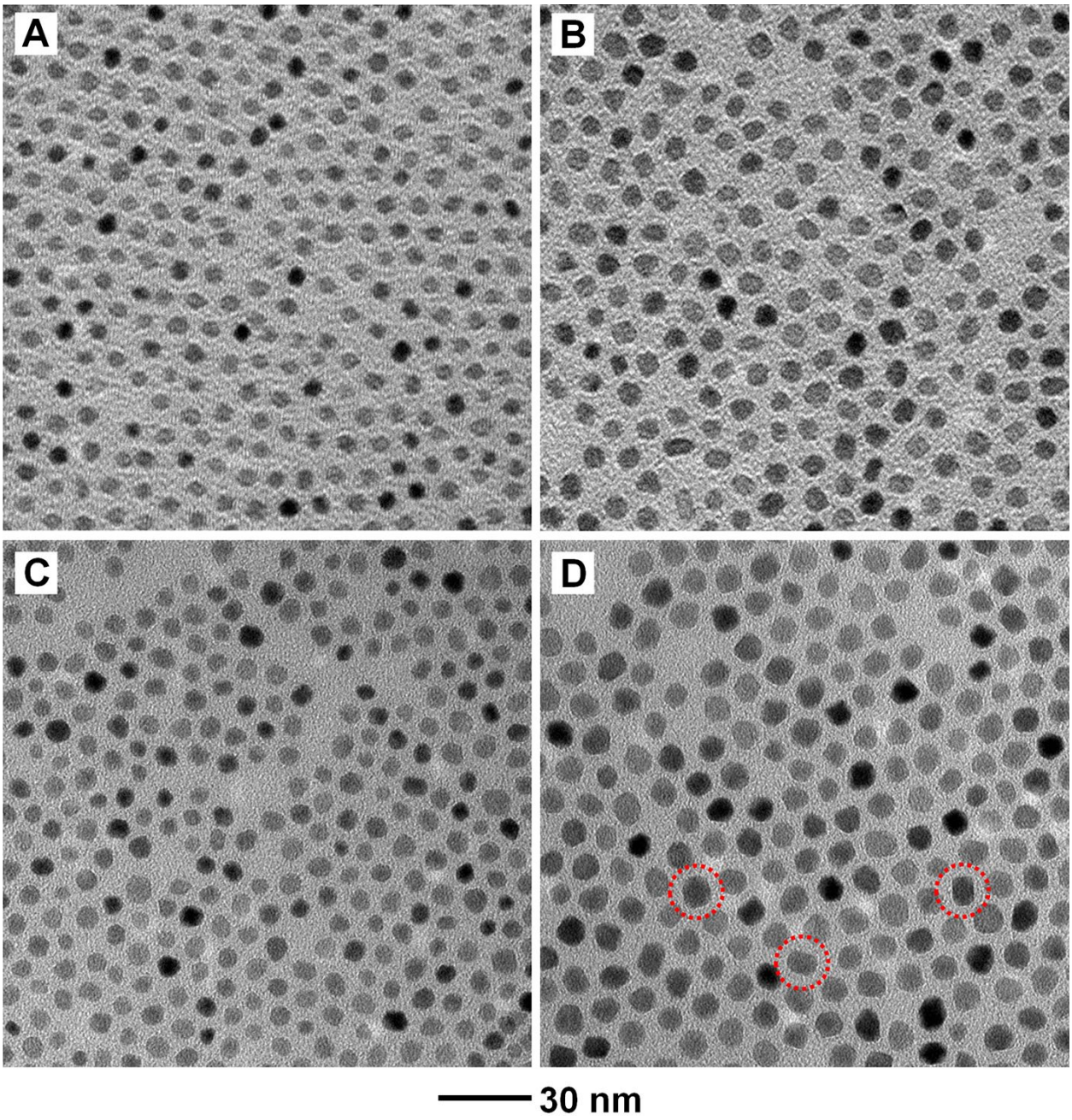

Fig. 2. TEM images of the Pt−Co nanocrystals prepared using the standard protocol, except for the variation in $Mn_2(CO)_{10}$ amount: (A) 240, (B) 180, (C) 120, and (D) 60 mg, respectively. When an inadequate amount of $Mn_2(CO)_{10}$ was used, Pt−Co truncated cubes were formed, as indicated by the red circles in (D).

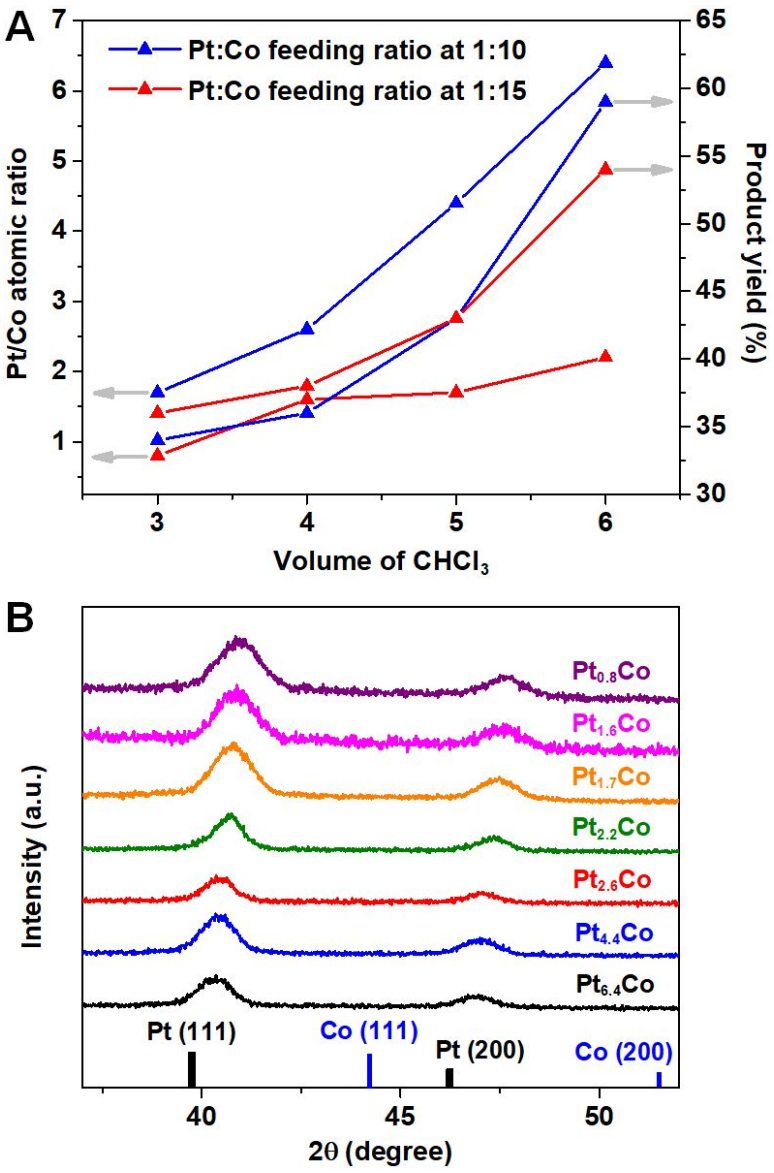

Fig. 3. (A) The Pt/Co atomic ratio and product yield as a function of the volume of $CHCl_3$ used in the standard syntheses of Pt−Co nanocrystals at two different Pt/Co molar feeding ratios of 1:10 (blue) and 1:15 (red), respectively. (B) XRD patterns of the Pt−Co nanocrystals with different compositions. The diffraction peaks were gradually shifted to higher 2θ values as the Pt content decreased from bottom to top. Black bars: JCPDS #04-0802 (Pt); Green bars: JCPDS #15-0806 (Co).

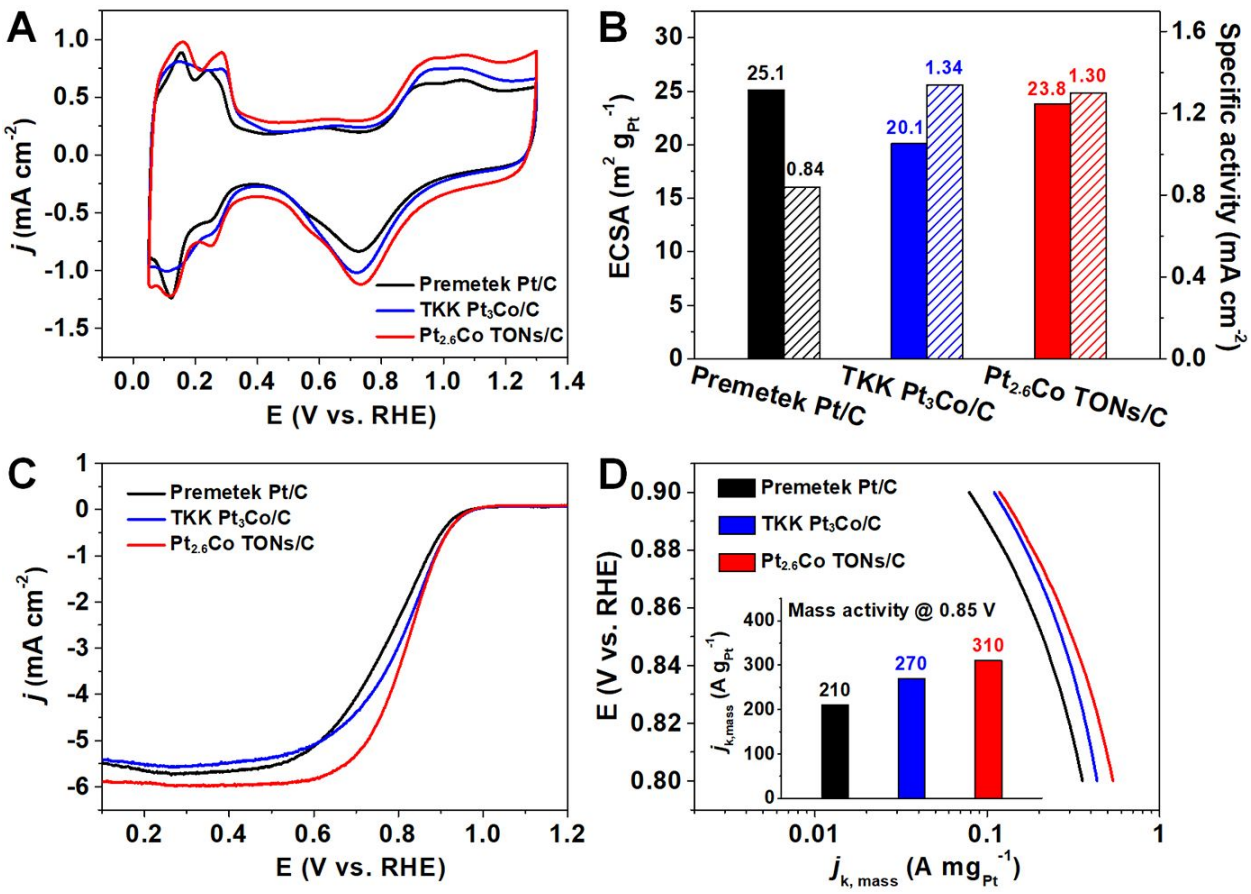

Fig. 4. Electrocatalytic properties of the 4-nm $Pt_{2.6}Co$ TONs/C catalyst in the liquid half-cell. (A) CV curves of the $Pt_{2.6}Co$ TONs/C, Premetek Pt/C, and TKK Pt_3Co/C catalysts in a N_2-saturated H_2SO_4. (B) Comparison of ECSAs (solid blocks) that were derived from the H_{UPD} charges and specific activity (hatched blocks) of the catalysts at 0.85 V *versus* RHE. (C) The positive-going ORR polarization curves of the catalysts in an O_2-saturated H_2SO_4 solution. The currents were normalized to the geometric area of the rotating disk electrode (0.196 cm^2). (D) Comparison of Pt mass activity of the catalysts at 0.85 V *versus* RHE. The Pt loadings for all catalysts were 10.2 μg cm^{-2} on the working electrodes.

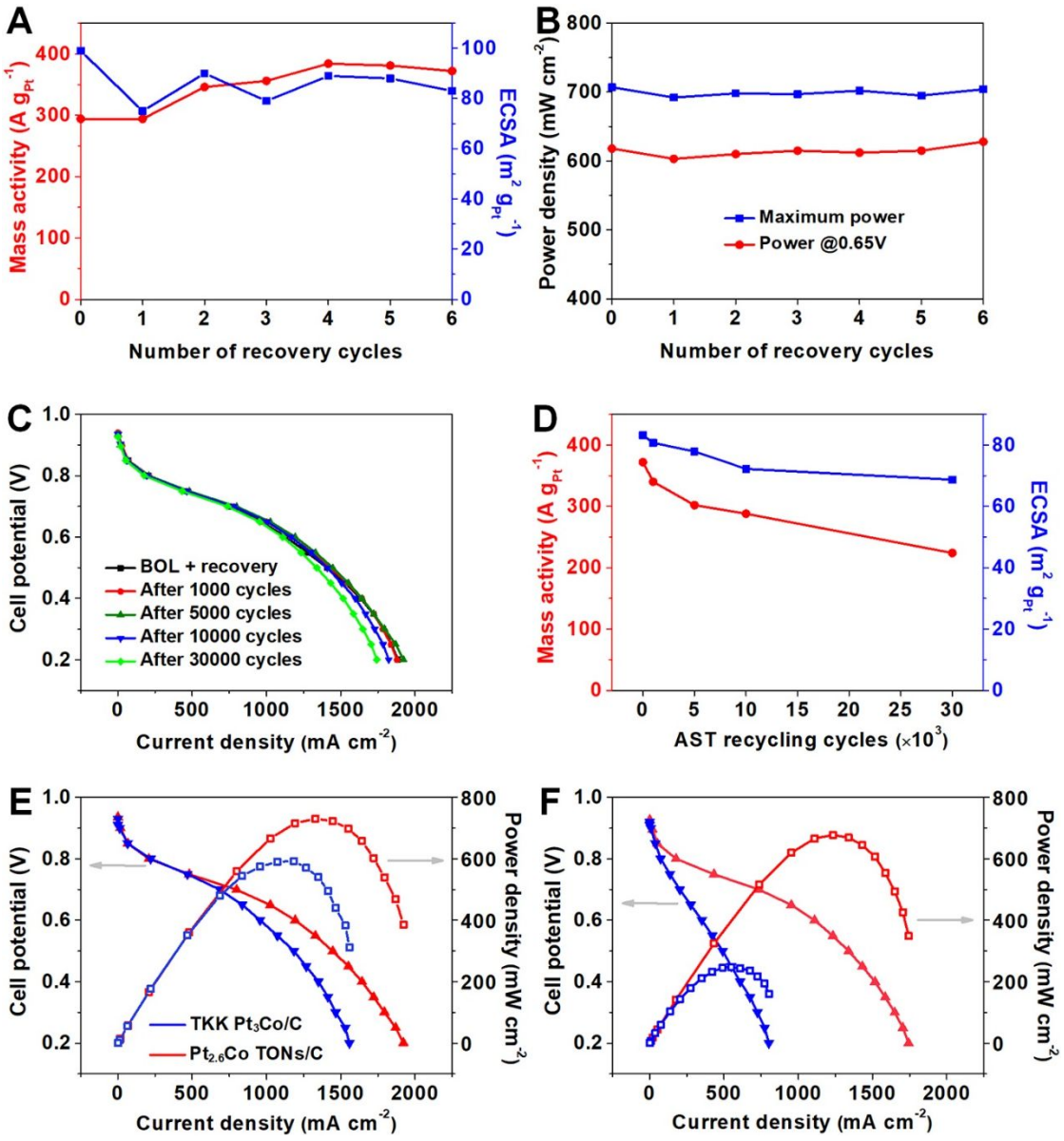

Fig. 5. MEA performance of the $Pt_{2.6}Co$ TONs/C catalyst in fuel cells. (A) Mass activity at 0.9 V *versus* RHE and ECSA. (B) Power densities of $Pt_{2.6}Co$ TONs/C as a function of the number of recovery cycles. (C) H_2/air fuel cell polarization curves recorded on a MEA of $Pt_{2.6}Co$ TONs/C (17.6 wt% Pt loading ratio, and the mass loading of Pt was 0.10 mg_{Pt} cm^{-2}) during the AST. (D) Mass activity and ECSA of $Pt_{2.6}Co$ TONs/C at different AST recycling cycles. (E, F) H_2/air fuel cell polarization curves and the corresponding power density curves of $Pt_{2.6}Co$ TONs/C (red) and TKK Pt_3Co/C (blue) at (E) BOL and (F) EOL (30,000 AST cycles).

Table of Contents Entry

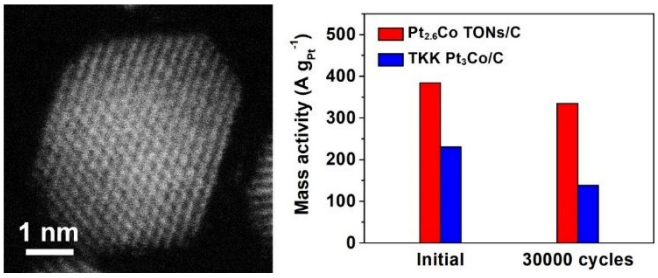

Pt−Co truncated octahedral nanocrystals were synthesized and evaluated as a class of highly active and durable catalysts toward oxygen reduction.